Nanoscale

Accepted Manuscript

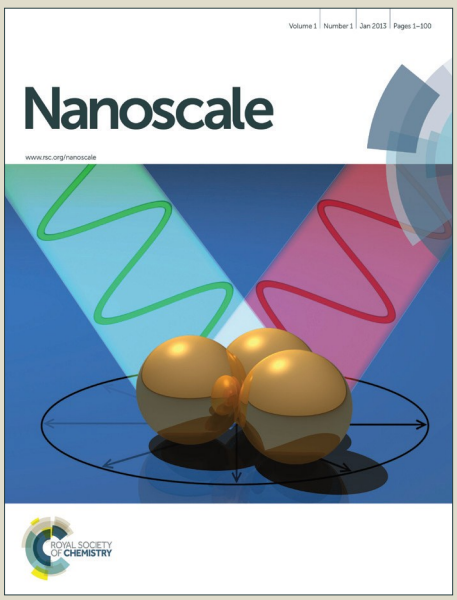

ROYAL SOCIETY OF CHEMISTRY

www.rsc.org/nanoscale

Co_3O_4-embedded porous ZnO rhombic dodecahedron prepared by the use of zeolitic imidazolate frameworks as precursors for CO_2 photoreduction

Tao Wang,*[ab] Li Shi,[a] Jing Tang,[a] Victor Malgras,[a] Shunsuke Asahin,[c] Guigao Liu,[a] Huabin Zhang,[a] Xianguang Meng,[a] Kun Chang,[a] Jianping He,[b] Osamu Terasaki,[d] Yusuke Yamauchi,[ae] and Jinhua Ye*[aef]

[a] World Premier International Research Center for Materials Nanoarchitectonics, National Institute for Materials Science, 1-1 Namiki, Tsukuba, Ibaraki 3050044, Japan

[b] College of Materials Science and Technology, Jiangsu Key Laboratory of Materials and Technology for Energy Conversion, Nanjing University of Aeronautics and Astronautics, Nanjing 210016, P. R. China

[c] JEOL Ltd., SM Business Unit, Tokyo, Japan

[d] Department of Materials and Environmental Chemistry, Berzelii Centre EXSELENT on Porous Materials, Stockholm University, SE-10691 Stockholm, Sweden

[e] TU-NIMS Joint Research Center, School of Materials Science and Engineering, Tianjin University, 92 Weijin Road, Tianjin, 300072, P.R. China

[f] Collaborative Innovation Center of Chemical Science and Engineering, Tianjin, 300072, P.R. China

***Corresponding Author:** wangtao0729@nuaa.edu.cn, Jinhua.YE@nims.go.jp

Keywords: metal–organic frameworks, porous metal oxides, ZnO@Co_3O_4 crystals, photocorrsion, photoreduction of carbon dioxide

Abstract: Metal−organic frameworks (MOFs) are attracting considerable attention as both the precursor and template to prepare metal oxides or carbon-based materials. For the first time in this paper, the core-shell ZIF-8@ZIF-67 crystals are thermally converted into porous ZnO@Co_3O_4 composites by combining a seed-mediated growth process with a two-step calcination. The designed porous ZnO@Co_3O_4 composites have exhibited the highest photocatalytic activity with an excellent stability for reduction of CO_2 among the commonly reported composite photocatalysts. The superior photocatalytic performance is demonstrated to be resulting from the unique porous structure of ZnO@Co_3O_4 and the co-catalytic function of Co_3O_4 which can effectively suppress the photocorrosion of ZnO.

1. Introduction

For decades, much effort has been devoted to the development of new researches for the photoreduction of CO_2, since fossil fuel shortage and global warming are problems which need to be addressed.[1-5] Metal oxides semiconductors with special morphology and porous features have received a lot of attention owing to their promising performance in the fields of energy and sustainability, especially heterogeneous photocatalysis and photovoltaic cell.[6-10] In particular, metal oxides semiconductors with a mesoporous structure have attracted growing interest for the conversion of CO_2 due to their interconnected porous network and high specific surface area which can effectively improve the diffusion of reactants, the separation of photogenerated charges, and the photocatalytic activity.[11-15] The most popular methods to construct porous structures are the template-engaged approaches, which have demonstrated effectiveness in forming porous metal oxide particles with various morphologies.[16-18] Nevertheless, the general template-engaged routes reported so far require tedious synthetic procedures, especially during the removal of the sacrificial template. Therefore, it is still a big

necessary to explore facile and reliable approaches for the large-scale synthesis of metal oxides with specifically designed morphology and porous structure which may bring about a great interest in the field of materials science.

Metal−organic frameworks (MOFs) and porous coordination polymers (PCP) are a novel class of porous materials consisting of metal ions coordinated with rigid organic molecules.[19,20] In recent years, MOFs have been proven to be a promising precursor/sacrificial template for the construction of corresponding morphology-inherited carbon or metal oxides.[21-23] In previous researches, nonporous metal oxide nanoparticulates have been generated via one-step calcination in an air atmosphere, because of the apt agglomeration of the metal oxide nanocrystals during the thermolysis of the MOFs.[24-26] Recent studies have shown that the control of the retention time and the evaporation rate of the organic moieties in the host solid were absolutely vital for the successful formation of nanoporous metal oxides with nanocrystalline frameworks.[27,28] For example, the manipulation of template-engaged reactions between the Prussian blue template and different alkaline substances have been established to simply lead to the formation of complex hollow microboxes on a large scale.[29] In addition, coordination polymer particles (CPPs) have been prepared by using a precipitation method where the cation exchange reaction is conducted for specific compositional transformations; the subsequent calcination leads to the decomposition of the CPPs and the formation of metal oxides.[30] Recently, hierarchical nanoporous metal oxides with tunable and highly nanocrystalline such as magnesia (MgO) and ceria (CeO_2), have been prepared via the thermolysis of aliphatic ligand-based MOFs.[31]

Zeolitic imidazolate frameworks (ZIFs) are popular porous MOFs, are porous materials with structures based on 4-connected nets of zeolites wherein the metal ion and imidazolate replace the tetrahedral Si nodes and the oxide bridges, respectively.[32] The common ZIFs, such as rhombic dodecahedral ZIF-67 ($[Co(2\text{-methylimidazole})_2]_n$, space group *I*-43*m*, a = 16.9589(3) Å, α= 90°; b = 16.9589(3) Å, β= 90°; c = 16.9589(3) Å, γ = 90°) and ZIF-8

($[Zn(2\text{-methylimidazole})_2]_n$, space group *I*-43*m*, a = 16.9910(12) Å, α= 90°; b = 16.9910(12) Å, β= 90°; c = 16.9910(12) Å, γ = 90°), have proved to be useful precursors for preparing various kinds of metal oxides.[30,33] For example, a ternary porous $Zn_xCo_{3-x}O_4$ hollow polyhedra was successfully prepared by thermally decomposing a heterobimetallic ZIFs template with a unique polyhedral morphology, leading to the coprecipitation of the Zn and Co ions in the presence of 2-methylimidazolate. The obtained $Zn_xCo_{3-x}O_4$ hollow polyhedra exhibited a high reversible electric capacity, excellent cycling stability, and good electrochemical rate capability when used as an anode material in lithium-ion batteries.[27] Another approach is annealing specific MOFs coated with three-dimensional graphene (3DGN) to prepare ZnO/3DGN the composites, which were used as a photocatalyst for the photodegradation methylene blue dyes under UV irradiation.[34]

Recently, Yamauchi *et al.* reported an original seed-mediated growth method to prepare core-shell ZIF-8@ZIF-67 crystals. Selectively functionalized carbon polyhedra, consisting of nitrogen-doped carbons as cores and highly graphitic carbon as shells, can be obtained after calcinating ZIF-8@ZIF-67 crystals under inert atmosphere.[35] In this study, we report for the first time the design and synthesis of two-component multifunctional metal oxides composite by combining a seed-mediated growth method and a two-step calcination process. The prepared porous ZnO@Co_3O_4 composite exhibits a much higher photocatalytic activity for CO_2 reduction compared to the commercial ZnO and TiO_2 (P25) powders due to the presence of the Co_3O_4 co-catalyst and the porous structure. More importantly, we demonstrate that Co_3O_4 is able to effectively reduce the photocorrosion of ZnO.

2. Experimental section

2.1 Preparation of ZIF-8-derived ZnO.

The ZIF-8 was synthesized according to a method reported by O. M. Yaghi *et al.*,[32] where white particles of ZIF-8 with a diameter of 350 nm are precipitated. Then the white powder is

pyrolyzed in a tubular furnace at 400 ^{o}C for 2 h under a N_2 atmosphere at a heating rate of 1 ^{o}C min^{-1} to obtain the ZnO precursor. Finally, the ZnO precursor is calcined at 400 ^{o}C for 2 h in an air atmosphere to obtain ZIF-8-derived ZnO. For comparison, we fabricated ZIF-8 derived ZnO which named ZnO-2 via one-step calcination of ZIF-8 at 400 ^{o}C for 2 h under an atmosphere at a heating rate of 1 ^{o}C min^{-1}.

2.2 Preparation of ZIF-8@ZIF-67-derived ZnO@Co_3O_4.

ZIF-8@ZIF-67 is synthesized according to a method reported by Y. Yamauchi *et al.*,[35] and the lilac particles with a diameter of 450 nm are precipitated. Then the lilac powder is pyrolyzed in a tubular furnace at 400 ^{o}C for 2 h under a N_2 atmosphere at a heating rate of 1 ^{o}C min^{-1} to obtain the ZnO@Co_3O_4 precursor. Finally, the ZnO@Co_3O_4 precursor is calcined at 400 ^{o}C for 2 h in air to obtain ZIF-8@ZIF-67-derived ZnO@Co_3O_4. We also prepared ZnO@Co_3O_4-500 and ZnO@Co_3O_4-600 at 500 or 600 ^{o}C for 2 h by calcinating ZnO@Co_3O_4 precursor. For comparison purposes, we fabricated ZIF-67-derived Co_3O_4 with a similar process to ZIF-8-derived ZnO.

2.3 Characterization.

X-ray diffraction (XRD) patterns were recorded on an X-ray diffractometer (Rint 2000, Altima III, Rigaku Co. Japan) using a Cu Kα_1 source. Nitrogen adsorption–desorption isotherms were measured at 77 K by using a BEL SORP-mini II (BEL Japan INC., Japan). The specific surface area of the photocatalysts was calculated by the Brunauer–Emmett–Teller (BET) method, and the total pore volume and the distributions were estimated by the Barrett–Joyner–Halenda (BJH) method through the adsorption branch. The transmission electron microscopy (TEM) analysis was conducted with a field-emission TEM (2100F, JEOL Co., Japan) operating at 200 kV. An energy dispersive X-ray spectrometer (EDX) installed in a 2100F was used to analyze the microzone composition (STEM-EDX mapping). The scanning electron microscopy (SEM) images were recorded on a field-emission SEM (S4800, Hitachi Co., Japan) with an acceleration voltage of 10 kV. The

low voltage high resolution SEM images of the fine structures were taken with the in-column detector of a JEOL JSM-7800F GBSH. The elemental chemical analysis of the samples was performed by X-ray photoelectron spectroscopy (XPS, PHI Quantera SXM, ULVAC-PHI Inc., Japan). Weight changes were monitored by using a TG/DTA instrument (DTG-60HDTA-TG, Shimadzu Co., Japan) from room temperature to 800 ^{o}C under N_2 or air with a heating rate of 1 ^{o}C min^{-1}.

2.4 Photocatalytic measurements.

All the photocatalysts were treated at 400 ^{o}C in O_2 for 4 h to remove organic adsorbates before the photoreduction of CO_2. In detail: A 300 W xenon arc lamp was used as the light source; 0.1 g of the photocatalyst was uniformly dispersed on a porous quartzose film in a reaction cell, and 3 mL of deionized H_2O and 80 KPa pure CO_2 gas were added into an airtight circulation system. The gaseous products were measured by using a gas chromatograph (GC-14B, Shimadzu Co., Japan). The isotope analysis of ^{13}C was carried out by using a gas chromatographmass spectrum (JEOL-GCQMS, JMS-K9 and 6890N Network GC system, Agilent Technologies).

3. Results and discussion

3.1 Synthesis and characterization of ZIFs-derived ZnO and ZnO@Co_3O_4.

The designed schematic route for fabricating ZIFs-derived ZnO and ZnO@Co_3O_4 composite is described in Fig. 1. Core-shell structured ZIF-8@ZIF-67 crystals are prepared through solvothermal method. Firstly, ZIF-8 is prepared at room temperature through a coordination reaction between zinc ions and 2-methylimidazole.[32] Then, the ZIF-8 seeds are coated with ZIF-67 by a solvothermal process to form the core-shell ZIF-8@ZIF-67 crystals, in which each single Zn^{2+} or Co^{2+} ion is connected with four 2-methylimidazole molecules.[35] In order to further assess the core-shell structure of ZIF-8@ZIF-67, low-voltage high-resolution scanning electron microscopy (SEM) image and elemental mapping analysis are performed

(Fig. 1), showing that the surface of Zn-based material is coated with a Co-based material. Finally, ZIF-8 and ZIF-8@ZIF-67 crystals are calcined by a two-step thermal treatment, thus yielding ZnO and ZnO@Co_3O_4 composite, respectively. Why did we choose the two-step thermal treatment process? Based on the TG/DTA results (Fig. S1a,b), by using the one-step calcination method in an air atmosphere, ZIF-8 started to be pyrolyzed at 300 ^oC and then rapidly lost weight at 373 ^oC, which leaded to formation of nonporous ZnO nanoparticulates (Fig. S2a). Thus, in this paper, the core-shell ZIF-8@ZIF-67 crystals are thermally converted to the porous ZnO@Co_3O_4 composites via a two-step calcination. Firstly, the core-shell ZIF-8@ZIF-67 crystals were pyrolyzed in a tubular furnace at 400 ^oC for 2 h under a N_2 atmosphere at a heating rate of 1 ^oC min^{-1} to obtain the ZnO@Co_3O_4 precursor. According to TG/DTA analysis (Fig. S1c,d), ZIF-8@ZIF-67 started to be pyrolyzed at 330 ^oC and leaded to the slight carbonization and weight loss. We can see the colour of obtained ZnO@Co_3O_4 precursor is grey-purple, whereas the colour of ZIF-8@ZIF-67 is purple. In addition, the morphology of ZnO@Co_3O_4 precursor is almost the same to ZIF-8@ZIF-67 (Fig. S2b). Then, the ZnO@Co_3O_4 precursor was calcined at 400 ^oC for 2 h under an air atmosphere to obtain ZIF-8@ZIF-67 derived ZnO@Co_3O_4. According to the TG/DTA analysis in air atmosphere (Fig. S1e,f), the ZnO@Co_3O_4 precursor pyrolyzed slowly before 400 ^oC, then the organics were completely removed at 400 ^oC and formed the target ZnO@Co_3O_4. Therefore, the final product ZnO@Co_3O_4 shows that the Co_3O_4 nanoparticles were embedded on the surface of the porous ZnO polyhedra. For comparison, porous Co_3O_4 is prepared by calcining ZIF-67 crystals, similarly to the preparation of ZnO derived from ZIF-8.

The crystal structure and morphology of the prepared ZIFs are analyzed by X-ray diffraction spectroscopy (XRD), SEM and transmission electron microscopy (TEM). As shown in Fig. 2a, the position of the diffraction peaks of the obtained ZIF-67, ZIF-8 and ZIF-8@ZIF-67 crystals correspond well to the patterns simulated from the single crystal structures of ZIF-67 or ZIF-8.[32,35] TEM (Fig. 2b) and SEM (Fig. 2c) images confirm that the

obtained white ZIF-8 powders consist of dispersed rhombic dodecahedral crystals with a uniform size of 350 nm. After carefully dispersing ZIF-8 seeds in methanol and adding a methanolic solution of $CoCl_2$ and MeIm units, a crystalline shell of purple ZIF-67 is grown on the surface of the ZIF-8 seed. The core-shell structured ZIF crystals (ZIF-8@ZIF-67) can also be observed on TEM elemental mapping images (Fig. 2d), revealing the layer of cobalt species homogeneously coated on the core of the zinc species. As shown in Fig. 2e and f, the size of the obtained ZIF-8@ZIF-67 increases up to 450 nm, and the crystals exhibit a similar dispersity and morphology to the ZIF-8 seeds.[35]

According to the XRD measurements (Fig. 3a), the calcination of ZIF-8 and ZIF-67 leads to the formation of hexagonal ZnO (JCPDS card #01-1136) and cubic Co_3O_4 (JCPDS card # 01-1152), respectively. For ZIF-8@ZIF-67 crystals, the calcined product consists in a combination of a main core phase (hexagonal ZnO) and a secondary shell phase (cubic Co_3O_4). X-ray photoelectron spectroscopy (XPS) is conducted to further ascertain the electronic configuration of the obtained compounds. Two forms of cobalt oxide, CoO and Co_3O_4, can be distinguished from the location of the satellite peaks from the XPS spectra.[36] As shown in Fig. S3a, a low satellite peak appears at a binding energy of 789.6 eV, which is about 9.9 eV higher than the peak of Co *2p3/2* (779.7 eV) and belongs to the typical satellite peak of Co_3O_4.[36] Because the typical satellite peak of CoO is only about 2.1 eV higher than the position of the main peak of Co *2p3/2*.[37] The electric states of Zn in the samples derived from ZIF-8 and ZIF-8@ZIF-67 were shown in Fig. S3b, and we can see that two characteristic peaks with respect to Zn $2p_{3/2}$ and Zn $2p_{1/2}$ confirm the Zn^{2+} state of ZnO in these samples.[38] From the results of XRD and XPS (Fig. 3a and Fig. S3), it demonstrates that the products derived from ZIF-67, ZIF-8 and ZIF-8@ZIF-67 are Co_3O_4, ZnO and ZnO@Co_3O_4, respectively.

The structure and morphology of the calcined metal oxides are observed by SEM and TEM. As shown in Fig. 3b-c and Fig. S4, the obtained ZnO particles have a porous structure

and retain the original rhombic dodecahedron shape from the parent ZIF-8. ZIF-8@ZIF-67 crystals were thermally converted to $ZnO@Co_3O_4$ in the same way. Can they remain the core-shell structure (The type of A as pictured in Fig. 1)? As revealed by SEM and TEM (Fig. 3d-f and Fig. S5), the obtained $ZnO@Co_3O_4$ composite consists of rhombic dodecahedron-shaped porous crystals, whose surfaces are decorated with nanoparticles. According to the elemental mapping images (Fig. 3g) along with the high resolution TEM images (Fig. S5c), the rhombic dodecahedron-shaped porous crystals are composed of ZnO, while the 25 nm nanoparticles are composed of Co_3O_4. The results indicate that the morphology of the obtained $ZnO@Co_3O_4$ composite correspond to the B type pictured in Fig. 1. To assess the porosity of the as-prepared $ZnO@Co_3O_4$ composite, ZIF-8-derived ZnO, ZIF-67-derived Co_3O_4 (Fig. S6), along with the commercial ZnO (Fig. S7), the N_2 adsorption–desorption isotherms are acquired (Fig. S8a) and the pore size distributions (Fig. S8b) of the samples are shown. The estimated structural parameters, including the specific surface area (S_{BET}), total pore volume (V_{total}) and the average pore size, are summarized in Table S1. In general, a higher the specific surface area contains more active sites.[39,40] We can clearly see from the Table S1 that the ZIFs derived metal oxides possess a higher specific surface area than that of commercial ZnO.

3.2 Photocatalytic reduction of CO_2 with ZIFs-derived ZnO and $ZnO@Co_3O_4$.

In order to evaluate the structural advantages of the ZIFs-derived porous metal oxides for CO_2 photoreduction, the photocatalytic reaction was carried out in a gas-closed circulation system in the presence of water vapor and CO_2. As shown in Fig. 4a and b, CO_2 is photoreduced into CH_4 and CO under UV–vis irradiation, and the amounts of CH_4 and CO generated by using ZIF-8-derived ZnO are much larger than that of the commercial ZnO and ZIF-67-derived Co_3O_4. After coating with Co_3O_4, $ZnO@Co_3O_4$ exhibits the highest activity among all the samples. As calculated according to how each compound evolved after 6 h (Fig. 4c), the rate of CH_4 generation using is 0.99 μmol g^{-1} h^{-1}, which is about 66 times higher than the

commercial ZnO (0.015 μmol g^{-1} h^{-1}) and 367 times higher than that of commercial TiO_2 (P25) (0.0027 μmol g^{-1} h^{-1}). The photocatalytic activity of ZnO@Co_3O_4 is compared with previously reported results under similar conditions (Table S2). In this study, due to the porous structural property and the effect of Co_3O_4 as co-catalyst, a superior photocatalytic performance can be achieved. In order to explore the source of C in CH_4 and CO, contrastive experiments were performed in the dark or under light irradiation in the absence of photocatalysts, CO_2 or water, and only negligible CH_4 or CO was detected. A more exact control experiment was performed by using $^{13}CO_2$ instead of $^{12}CO_2$ (GC–MS are shown in Fig. S9). The main peak with a retention time from 02:50-03:45 min is confirmed to be $^{13}CO_2$. The two other peaks with retention times of 02:06 and 02:19 min are the main products: O_2, CO and CH_4. Moreover, the main organic product CO and CH_4 are verified to be ^{13}CO and $^{13}CH_4$. Therefore, the results of the above experiments demonstrate that the source of C in CH_4 and CO was generated from CO_2 through a photocatalytic process.

In order to study how the calcination temperature affects the photocatalytic activity, we prepared ZnO@Co_3O_4 in different temperature (400, 500 and 600 °C). In general, the size of the ZnO grain increases with the calcination temperature. As expected, the average crystalline sizes of ZnO in ZnO@Co_3O_4-400, ZnO@Co_3O_4-500, and ZnO@Co_3O_4-600 estimated from Scherrer equation ($D = k\lambda/\beta\cos\theta$) via XRD (Fig. S10) are 12.0, 22.1 and 40.2 nm, respectively, which is in good agreement with the results of TEM images (Fig. S5c and S11). That is to say, as the calcination temperature increases, the crystalline sizes increase and lead to the structural collapse of the porous rhombic dodecahedron. In the end, the specific surface area reduces and the pore size distribution weakens or disappears (Fig. S12). As we know, the larger the specific surface area of photocatalysts, the higher the photocatalytic activity.[12,13,41] Fig. S13 clearly shows that CO_2 is photoreduced to CH_4 and CO under UV-vis light, and the generated rate of products decreases with the increased calcination temperature. Therefore,

the sequence of photocatalytic activity for CO_2 reduction is ZnO@Co_3O_4-400 > ZnO@Co_3O_4-500 > ZnO@Co_3O_4-600, in accordance with the specific surface area.

Further investigating the photocatalytic stability is necessary. As shown in Fig. 4a and b, the CO evolution of the ZIF-8-derived ZnO is stable, while the CH_4 evolution slows down after 7 h. When the ZnO is coated with Co_3O_4 nanoparticles, the stability is enhanced (Fig. 4b). One could wonder why ZnO@Co_3O_4 possesses better photocatalytic stability than the ZnO. It is well known that photocorrosion of ZnO, which reduces the photocatalytic stability of ZnO, occurs easily. The changes in the main phase composition and in the structure caused by the photocatalytic reaction are investigated by XRD, XPS and TEM. Before the photocatalytic reaction (Fig. 5a and b), the commercial ZnO and the ZIF-8-derived ZnO have a hexagonal ZnO crystal structure (JCPDS card #01-1136), while after, both of them have a rhombohedral $ZnCO_3$ structure (JCPDS card #03-0774). In the case of ZnO@Co_3O_4, there is no obvious change after the photocatalytic reaction (Fig. 5c). The C *1s* XPS patterns (Fig. 5d-f) of the samples also show that CO_3^{2-} (~289 eV) is present in both the commercial ZnO and ZIF-8-derived ZnO, but cannot be detected in the ZnO@Co_3O_4 after the photocatalytic reaction.

Furthermore, we observe by TEM a change in the morphology of ZnO and ZnO@Co_3O_4 following the photocatalytic reaction (Fig. 6a-d). The TEM images show that the morphology of ZnO has been destroyed, while the morphology of ZnO@Co_3O_4 is well-retained. The proposed ideal reaction equations for the photoreduction of CO_2 by ZnO under UV-vis irradiation are depicted in Fig. S14a (1, 2, 3). XRD and XPS analysis suggest, however, the appearance of $ZnCO_3$ (Fig. 5) and the instability of the CH_4 evolution (Fig. 4b) after the photocatalytic reaction. That is to say, the photocorrosion of ZnO occurs and the actual reaction equations are as presented in Fig. S14a (1, 4, 5), which result in the instability of the CH_4 evolution. On the other hand, there is no obvious change after the photocatalytic reaction for the ZnO@Co_3O_4, indicating that the reaction equations for the photoreduction of CO_2 with

$ZnO@Co_3O_4$ under UV-vis irradiation are as proposed in Fig. S14b and Co_3O_4 protects ZnO from photocorrosion. Co_3O_4, which is often used as an effective water oxidation co-catalyst,[15,42,43] could further promote the holes transferring from ZnO to Co_3O_4.[44,45] Therefore, the schematic illustration of the photocatalytic CO_2 reduction with ZnO and $ZnO@Co_3O_4$ are shown in Fig. 6e and f. The ZnO particles are oxidized by holes to generate O_2 and Zn ions, followed by the reaction between the Zn ions and CO_2 to generate CO and $ZnCO_3$. In the case of the $ZnO@Co_3O_4$ composites, Co_3O_4 effectively protects ZnO from photocorrosion, leading to a more stable photocatalytic activity.

4. Conclusion

We have designed a convenient approach to prepare a novel porous $ZnO@Co_3O_4$ composite by using core-shell ZIF-8@ZIF-67 crystals as the precursor, and by combining a seed-mediated solvothermal process with a two-step calcination. The photocatalytic reduction of CO_2 shows that the advantageous porous structure of $ZnO@Co_3O_4$ and the co-catalytic properties of ZnO coated with Co_3O_4 can lead to a superior photocatalytic performance. The generated rate of CH_4 over $ZnO@Co_3O_4$ is 0.99 μmol g^{-1} h^{-1}, which is about 66 times higher than the commercial ZnO and 367 times higher than that of commercial TiO_2 (P25). Moreover, Co_3O_4 can effectively hinder the photocorrosion of ZnO and thus can enhance its photocatalytic stability. It is anticipated that the convenient method reported in this study can functionalize a multitude of MOFs with diverse metal oxides and extends to the fabrication of new artificially designed nanocomposites.

Acknowledgements

This work received financial support from the World Premier International Research Center Initiative (WPI Initiative) on Materials Nanoarchitectonics (MANA), MEXT, Japan, and the National Basic Research Program of China (973 Program, 2014CB239301).

Electronic supplementary information (ESI) available: Additional TG and DTA curves, XRD patterns, SEM images, TEM images, N_2 adsorption-desorption isotherms, X-ray photoelectron spectroscopy and GC-MS spectra of the samples. See DOI:

Notes and references

1. S. C. Roy, O. K. Varghese, P. Maggie and C. A. Grimes, *ACS Nano,* 2010, **4**, 1259–1278.

2. R. D. Richardson, E. J. Holland and B. K. Carpenter, *Nat. Chem.,* 2011, **3**, 301–303.

3. S. N. Habisreutinger, L. Schmidt-Mende and J. K. Stolarczyk, *Angew. Chem. Int. Ed.,* 2013, **52**, 7372–7408.

4. W. Tu, Y. Zhou and Z. Zou, *Adv. Mater.,* 2014, **26**, 4607–4626.

5. J. Yu, J. Low, W. Xiao, P. Zhou and M. Jaroniec, *J. Am. Chem. Soc.,* 2014, **136**, 8839–8842.

6. B. T. Holland, C. F. Blanford and A. Stein, *Science,* 1998, **281**, 538–540.

7. Y. Wang, X. Wang and M. Antonietti, *Angew. Chem. Int. Ed.,* 2012, **51**, 68–89.

8. X. Wang, J. Yu, C. Ho, Y. Hou and X. Hu, *Langmuir,* 2005, **21**, 2552–2559.

9. J. Yu, L. Zhang, B. Cheng and Y. Su, *J. Phys. Chem. C,* 2007, **111**, 10582–10589.

10. U. Bach, D. Lupo, P. Comte, J. Moser, F. Weissortel, J. Salbeck, H. Spreitzer and M. Gratzel, *Nature,* 1998, **395**, 583–585.

11. V. P. Indrakanti, J. D. Kubicki and H. H. Schobert, *Energ. Environ. Sci.,* 2009, **2**, 745–758.

12. S. Yan, S. Ouyang, J. Gao, M. Yang, J. Feng, X. Fan, L. Wan, Z. Li, J. Ye, Y. Zhou and Z. Zou, *Angew. Chem. Int. Ed.,* 2010, **49**, 6400–6404.

13. T. Wang, X. Meng, P. Li, S. Ouyang, K. Chang, G. Liu, Z. Mei and J. Ye, *Nano Energy,* 2014, **9**, 50–60.

14. M. Zeng, Y. Li, M. Mao, J. Bai, L. Ren and X. Zhao, *ACS Catal.,* 2015, **5**, 3278–3286.

15. T. Wang, X. Meng, G. Liu, K. Chang, P. Li, Q. Kang, L. Liu, M. Li, S. Ouyang and J. Ye, *J. Mater. Chem. A,* 2015, **3**, 9491–9501.

16. A. Imhof and D. J. Pine, *Nature,* 1997, **389**, 948–951.

17. D. M. Antonelli and J. Y. Ying, *Angew. Chem. Int. Ed.,* 1995, **34**, 2014–2017.

18. P. D. Yang, D. Y. Zhao, D. I. Margolese, B. F. Chmelka and G. D. Stucky, *Nature,* 1998, **396**, 152–155.

19 O. M. Yaghi, M. O'Keeffe, N. W. Ockwig, H. K. Chae, M. Eddaoudi and J. Kim, *Nature,* **2003**, *423*, 705–714.

20 S. Kitagawa, R. Kitaura and S. Noro, *Angew. Chem. Int. Ed.,* **2004**, *43*, 2334–2375.

21. B. Liu, H. Shioyama, T. Akita and Q. Xu, *J. Am. Chem. Soc.,* 2008, **130**, 5390–5391.

22. M. Hu, J. Reboul, S. Furukawa, N. L. Torad, Q. M. Ji, P. Srinivasu, K. Ariga,; S. Kitagawa and Y. Yamauchi, *J. Am. Chem. Soc.,* 2012, **134**, 2864–2867.

23. L. Zhang, H. B. Wu, S. Madhavi, H. H. Hng and X. W. Lou, *J. Am. Chem. Soc.,* 2012, **134**, 17388–17391.

24. X. Xu, R. Cao, S. Jeong and J. Cho, *Nano Lett.*, 2012, **12**, 4988-4991.

25. R. Das, P. Pachfule, R. Banergee and P. Poddar, *Nanoscale*, 2012, **4**, 591-599.

26. W. Cho, S. Park and M. Oh, *Chem. Commun.*, 2011, **47**, 4138-4140.

27. R. Wu, X. Qian, K. Zhou, J. Wei, J. Lou and P. M. Ajayan, *ACS Nano,* 2014, **8**, 6297–6303.

28. R. R. Salunkhe, J. Tang, Y. Kamachi, T. Nakato, J. H Kim and Y. Yamauchi, *ACS Nano*, 2015, **9**, 6288-6296.

29. L. Zhang, H. B. Wu and X. W. Lou, *J. Am. Chem. Soc.,* 2013, **135**, 10664–10672.

30. W. Cho, Y. H. Lee, H. J. Lee and M. Oh, *Adv. Mater.,* 2011, **23**, 1720–1723.

31. T. K. Kim, K. J. Lee, J. Y. Cheon, J. H. Lee, S. H. Joo and H. R. Moon, *J. Am. Chem. Soc.,* 2013, **135**, 8940–8946.

32. K. S. Park, Z. Ni, A. P. Cote, J. Y. Choi, R. Huang, F. J. Uribe-Romo, H. K. Chae, M. O'Keeffe and O. M. Yaghi. *Proc. Natl. Acad. Sci. U. S. A.,* 2006, **103**, 10186–10191.

33. R. Banerjee, A. Phan, B. Wang, C. Knobler, H. Furukawa, M. O'keeffe and O. M. Yaghi, *Science,* **2008**, *319*, 939–943

34. X. Cao, B. Zheng, X. Rui, W. Shi, Q. Yan and H. Zhang, *Angew. Chem. Int. Ed.,* 2014, **53**, 1404–1409.

35. J. Tang, R. R. Salunkhe, J. Liu, N. L. Torad, M. Imura, S. Furukawa and Y. Yamauchi, *J. Am. Chem. Soc.,* 2015, **137**, 1572–1580.

36. E. Comini, A. Cusma, S. Kaciulis, S. Kandasamy, G. Padeletti, L. Pandolfi, G. Sberveglieri, A. Trinchi and W. Wlodarski, *Surf. Interface Anal.,* 2006, **38**, 736–739.

37. N. S. Mclntyre and M. G. Cook, *Anal. Chem.,* 1975, **47**, 2208–2213.

38. B. R. Strohmeier and D. M. Hercules, *J. Catal.,* **1984**, *86*, 266–279.

39. W. Kowbel and C. H. Shan, *Carbon,* 1990, **28**, 287–299.

40. U. Gelius, P. F. Hedén, J. Hedman, B. J. Lindberg, R. Manne, R. Nordberg, C. Nordling and K. Siegbahn, *Physica Scripta,* 1970, **2**, 70.

41. X. Meng, S. Ouyang, T. Kako, P. Li, Q. Yu, T. Wang, J. Ye, *Chem. Commun.*, 2014, **50**, 11517-11519.

42. M. Liao, J. Feng, W. Luo, Z. Wang, J. Zhang, Z. Li, T. Yu and Z. Zou, *Adv. Funct. Mater.*, 2012, **22**, 3066–3074.

43. M. Barroso, A. J. Cowan, S. R. Pendlebury, M. Grätzel, D. R. Klug and J. R. Durrant, *J. Am. Chem. Soc.*, 2011, **133**, 14868–14871.

44. M. Li, K. Chang, T. Wang, L. Liu, H. Zhang, P. Li and J. Ye, *J. Mater. Chem. A*, 2015, **3**, 13731–13737.

45. Y. Tak and K. Yong, *J. Phys. Chem. C*, 2008, **112**, 74–79.

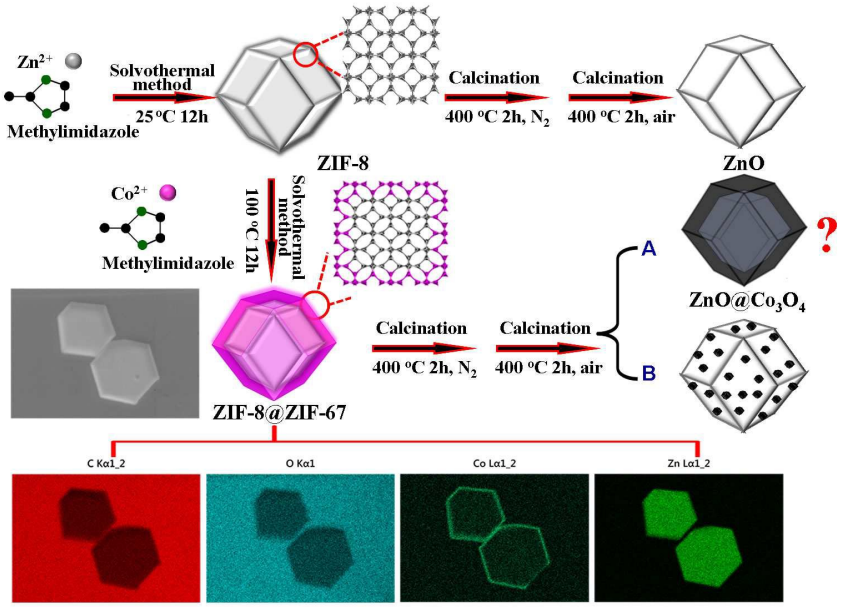

Fig. 1 Schematic illustration of the preparation of ZIF-8-derived ZnO and ZIF-8@ZIF-67-derived ZnO@Co_3O_4 polyhedron, and the SEM elemental mapping of C (K-line) in red, and O (K-line) in blue, Co (L-line) in aquamarine blue and Zn (L-line) in green, taken at acceleration voltage 30 kV for ZIF8@ZIF-67 crystals.

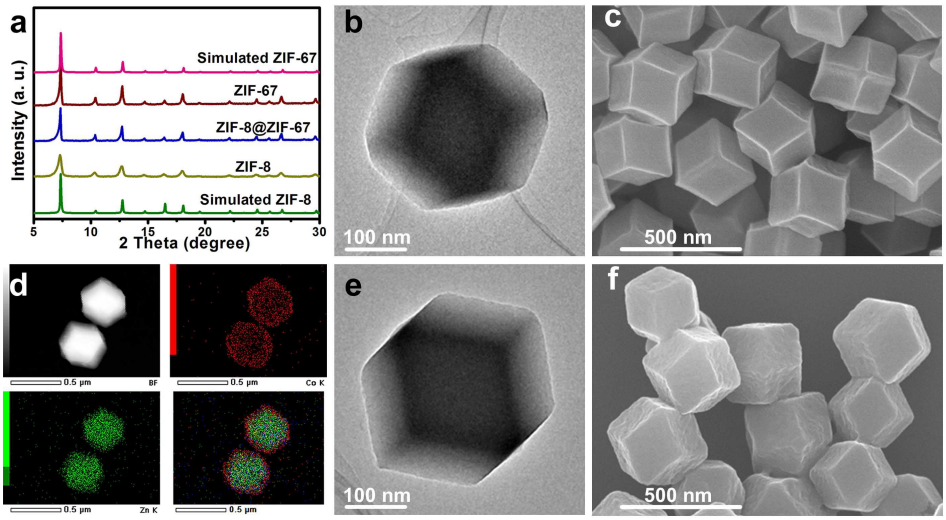

Fig. 2 (a) XRD patterns (λ = 0.15418 nm) of the as-prepared ZIF-67, ZIF-8 and core-shell ZIF-8@ZIF-67 samples and the simulated XRD patterns of ZIF-67 and ZIF-8 crystals; (b) TEM and (c) SEM images of ZIF-8 crystals; (d) EDS mapping of Co (K-line) in red, and Zn (K-line) in green taken at acceleration voltage 200 kV for core-shell ZIF-8@ZIF-67 crystals; (e) TEM and (f) SEM images of core-shell ZIF-8@ZIF-67 crystals.

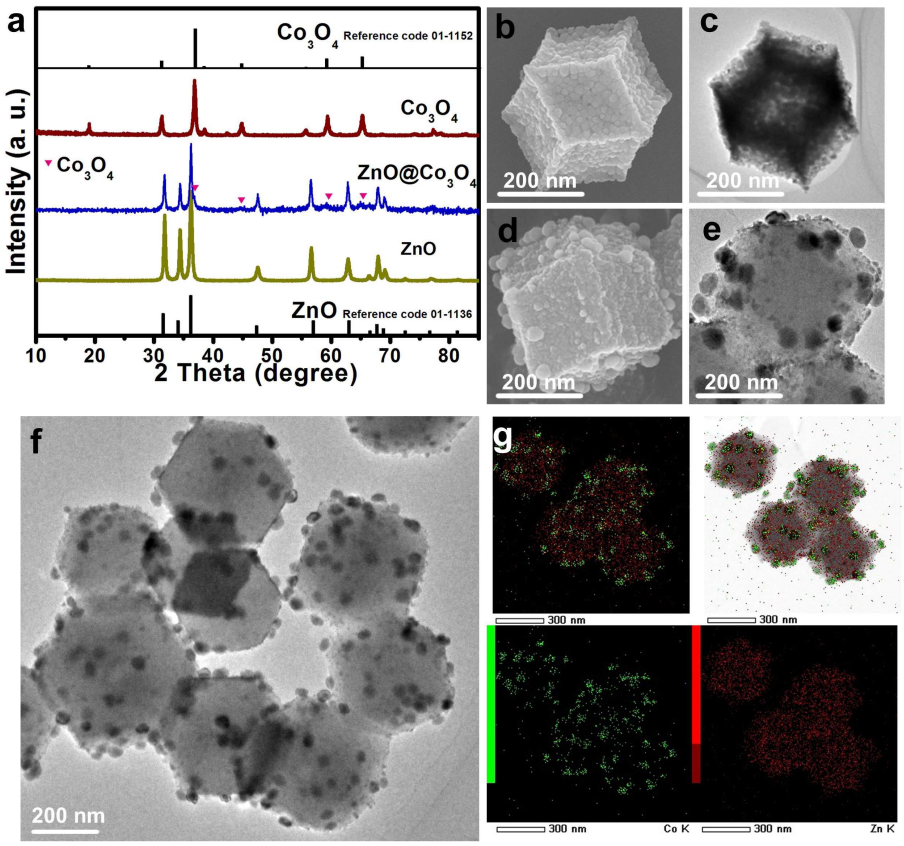

Fig. 3 (a) XRD patterns (λ = 0.15418 nm) of the Co_3O_4, ZnO and ZnO@Co_3O_4 samples prepared from ZIF-67, ZIF-8 and ZIF-8@ZIF-67, respectively; (b) SEM and (c) TEM images of ZnO prepared from ZIF-8; (d) SEM, (e,f) TEM of ZnO@Co_3O_4 prepared from ZIF-8@ZIF-67; (g) EDS mapping of Co (K-line) in red, and Zn (K-line) in green taken at acceleration voltage 200 kV for ZnO@Co_3O_4 prepared from ZIF-8@ZIF-67.

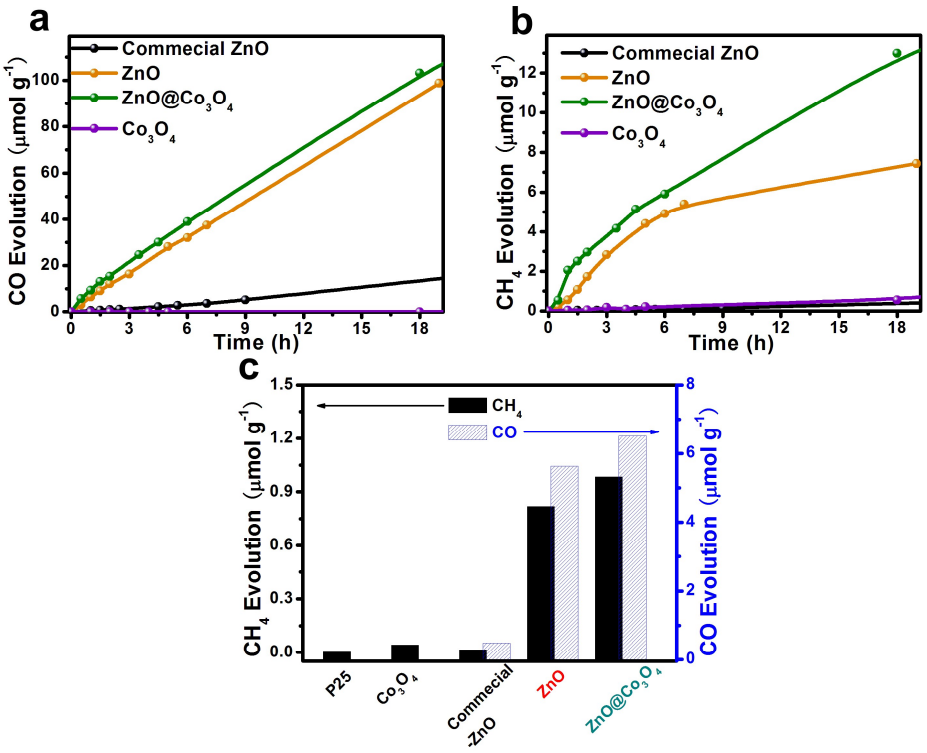

Fig. 4 (a) CO and (b) CH_4 evolution over various samples under UV-vis irradiation. (c) Comparison of the photocatalytic activity of the photocatalysts under UV-vis irradiation, calculated according to how each compound evolved after 6 h.

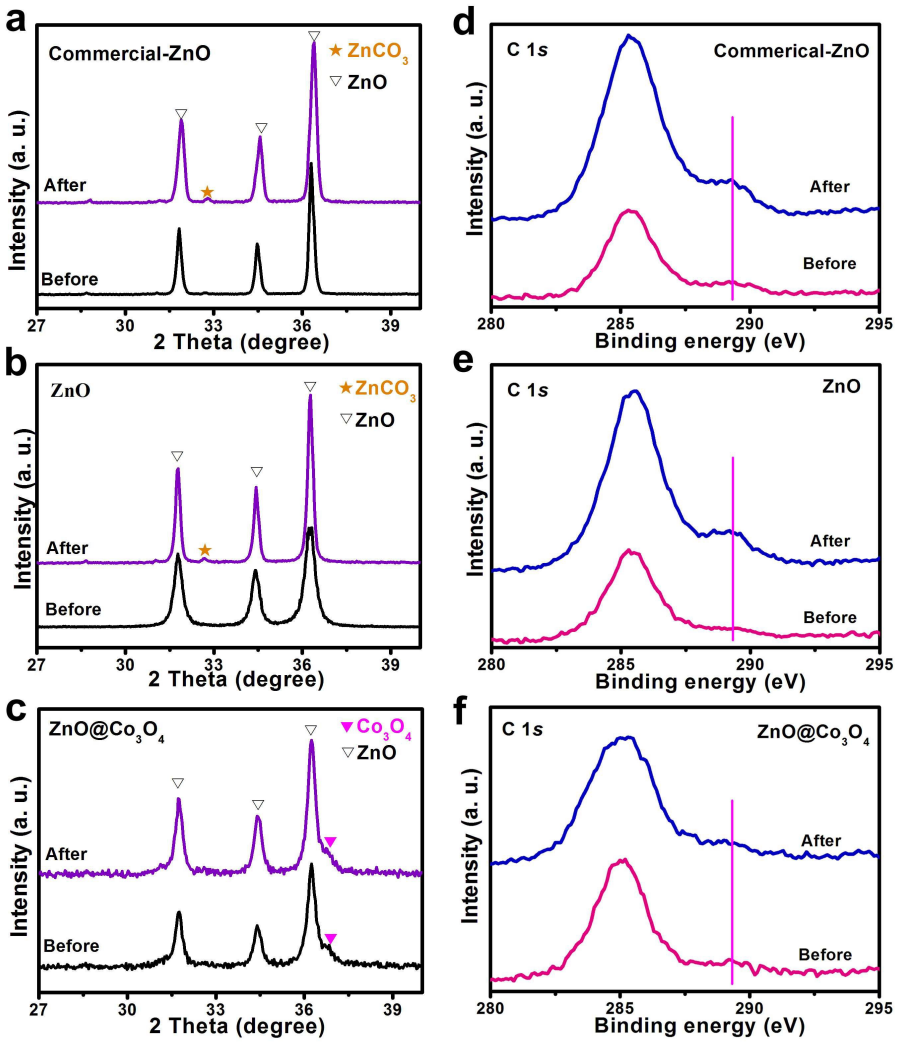

Fig. 5 (a, b, c) XRD (λ = 0.15418 nm) and (d, e, f) C1s XPS patterns of the commercial ZnO, ZIF-8-derived ZnO and ZnO@Co_3O_4 before and after photocatalytic CO_2 reduction.

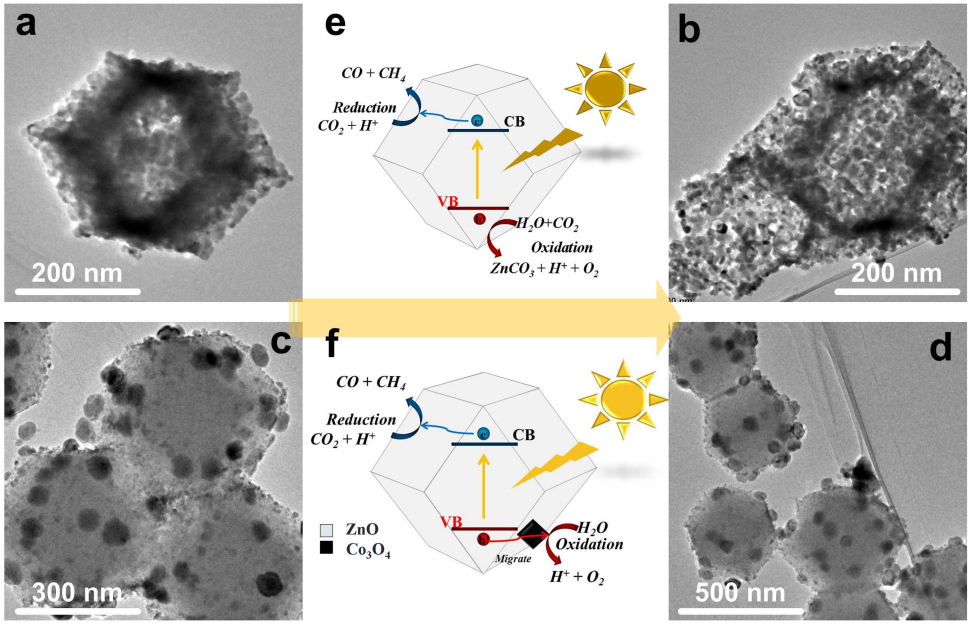

Fig. 6 TEM images of ZnO prepared from ZIF-8: (a) before and (b) after photocatalytic CO_2 reduction. TEM images of ZnO@Co_3O_4 prepared from ZIF-8@ZIF-67: (c) before and (d) after photocatalytic CO_2 reduction. Schematic illustration of the photocatalytic CO_2 reduction with (e) ZnO and (f) ZnO@Co_3O_4.